PHYSICAL REVIEW B **100**, 064420 (2019)

# Maximal tunnel magnetoresistance in magnetic nanoparticle arrays with perpendicular anisotropy

Arunkumar Bupathy,[1] Varsha Banerjee,[1] and Julian Carrey[2]
[1] *Department of Physics, Indian Institute of Technology, Hauz Khas, New Delhi–110016, India*
[2] *Université de Toulouse, INSA, UPS, Laboratoire de Physique et Chimie des Nano-Objets (LPCNO), 135 Avenue de Rangueil, F-31077 Toulouse, France*

(Received 28 January 2019; revised manuscript received 20 July 2019; published 26 August 2019)

We study tunnel magnetoresistance (TMR) ratio of self-assembled $2d$ magnetic nanoparticle (MNP) arrays by modeling them as interacting dipoles on a triangular lattice, which is representative of experimentally obtained assemblies. Low-temperature Monte Carlo simulations are performed to understand the effects of dipolar interactions and uniaxial anisotropy on TMR behavior. In magnetic tunnel junctions with a perfect antiparallel state, the TMR amplitude reaches the ideal value $2P^2/(1-P^2)$, where $P$ is the spin polarization. We show that, for MNPs with their anisotropy axes perpendicular to the array, the TMR amplitude can reach a value as large as 2400%, which represents an order of magnitude improvement over previous studies. We evaluate the conditions for which these large amplitudes could be obtained experimentally at room temperature and find that spherical MNPs with large magnetocrystalline anisotropy or nanorods are suitable candidates. Our theoretical results should stimulate experimental groups into elaborating the samples proposed in this work, which could display large TMR amplitudes.

DOI: 10.1103/PhysRevB.100.064420

## I. INTRODUCTION

Self-assembled magnetic nanoparticle (MNP) arrays are receiving a lot of interest due to their potential applications in high-density storage devices, switches, and magnetic field sensors [1–5]. They are usually functionalized with an insulating surfactant layer to prevent aggregation which, in the context of electrical conduction, acts as a tunnel barrier. Thus, the conductivity occurs via spin-dependent tunneling which forms the basis of several spintronic devices. The quantity used to characterize their electrical properties is the tunnel magnetoresistance (TMR) ratio. A widely used model for the evaluation of TMR is that by Inoue and Maekawa [6]. In this model, the conductance between a pair of moments $\vec{s}_i$ and $\vec{s}_j$ is given by

$$\sigma_{ij} \propto (1 + P^2 \cos\theta_{ij}), \tag{1}$$

where $\theta_{ij}$ is the angle between $\vec{s}_i$ and $\vec{s}_j$ and $P$ is the spin polarization of the conduction electrons. The resultant change in conductance on application of a magnetic field $H$ is quantified by the TMR ratio [6–8]

$$\mathrm{MR}^{\dagger}(H) = \frac{\sigma(H_s) - \sigma(H)}{\sigma(H)} = \frac{R(H) - R(H_s)}{R(H_s)}, \tag{2}$$

where $\sigma(H)$ is the total conductance of the array at an applied field $H$, $R$ is the resistance of the array, and $H_s$ is the field at which the conductance is maximized (this definition is slightly different from the one that we shall use later.) An antiferromagnetic configuration ($\cos\theta_{ij} = -1$) yields a maximum change in conductance on application of a field and hence the maximum TMR ratio. A ferromagnetic configuration of moments ($\cos\theta_{ij} = 1$), on the other hand, is the least favorable. For a given $P$, the theoretical maximum of the TMR amplitude is $2P^2/(1-P^2)$. For $P = 1$, Eq. (2) yields a maximum TMR amplitude of $\infty$ and a minimum of 0. However, as we shall see shortly, the TMR amplitudes obtained in experiments are far from this ideal value.

In closely packed MNP assemblies, the magnetic moments interact via strong dipole-dipole interactions. The latter are long ranged, anisotropic, and alternating in sign and have deep implications on the systemic behavior. Studies on MNP arrays have demonstrated interesting and far-reaching consequences of these interactions such as unusual ground-state ordering [9–11], complex remanence and coercivity behavior [11–13], increased blocking temperature [14], and glassy magnetization dynamics [14,15]. Consequently, the TMR response, which is itself a function of the spin state, is affected as well.

Many groups have studied the role played by dipolar interactions on the TMR behavior. Kechrakos and Trohidou performed Monte Carlo (MC) simulations of triangular arrays of cobalt MNPs with random anisotropy axes [7]. They modeled the arrays using resistor networks to obtain the conductance and TMR. The crucial results of their study are as follows: (i) the TMR amplitude decreases with increasing dipolar strength and (ii) in the limit of zero dipolar strength, the maximum TMR that can be achieved is $P^2$. Further, the sensitivity of TMR response was found to depend on the direction of the applied field. Similar conclusions were reached by Tan *et al.*, who used Landau-Lifshitz-Gilbert (LLG) equations to model the magnetization dynamics of such arrays [16]. On the other hand, MC simulations by Mao and Chen on hexagonal arrays with positional disorder showed a TMR response which was roughly independent of dipolar strength [17]. They also studied the effect of aligned anisotropy axes and found that the distribution of anisotropy axes only affected the sensitivity of the TMR response. In a more recent study using LLG methods, we have shown that an increase in aspect ratio of the array leads to a destruction of the TMR effect, which is related to the formation of flux loops and ferromagnetic chains [18].

In all these studies, the maximum TMR amplitude achieved was $P^2$, corresponding to the noninteracting case with random spin orientations. This is due to the fact that dipolar fields in triangular/hexagonal arrays tend to align the moments ferromagnetically. This greatly reduces their zero-field resistivity and hence the TMR response. For square lattices, however, a perfect antiferromagnetic state can be obtained by aligning the anisotropy axes perpendicular to the plane, and hence a perfect TMR value of $2P^2/(1-P^2)$ can be obtained [8] but, experimentally, it is difficult to obtain such square arrays. In any case, in experiments on self-assembled MNPs, nobody has so far attempted to elaborate samples with aligned anisotropy axes, and hence the typical TMR amplitude observed is quite small [2,19–23].

In this paper, we perform comprehensive low-temperature MC simulations on a triangular lattice to understand the twin effects of dipole-dipole interactions and the anisotropy energy on spin morphologies and their consequence on TMR. We provide a pathway, using MNP arrays with perpendicular anisotropy, to achieve maximal TMR amplitude in the experimentally relevant triangular lattices. We show that, for MNPs with their anisotropy axes perpendicular to the array, the TMR amplitude can reach a value as large as 2400%, which represents an order of magnitude improvement over previous studies. This paper is organized as follows. In Sec. II, we present the model and the methods used to study the MNP arrays. In Sec. III, we present our numerical results on the morphologies and TMR, and provide suggestions for best materials and parameter values for TMR-based applications. Finally, we end the paper with a summary of our results in Sec. IV.

## II. MODEL AND METHODS

### A. Model

Consider $N$ functionalized MNPs on a $L_x \times L_y$ triangular lattice, representative of typical assemblies obtained in deposition experiment. Let the lattice constant be $a$ and the particle core diameter be $d$. The edge-to-edge separation $s = a - d$ and is equal to the thickness of the tunnel barrier (i.e., the surfactant coating). Each MNP $i$ has a moment $\vec{\mu}_i = \mu \hat{s}_i$, where $\mu = M_s V$ is its magnitude, $\hat{s}_i$ is its direction (spin), $M_s$ is the saturation magnetization, and $V$ is the MNP volume. The total energy of this assembly in a uniform magnetic field can be expressed as [24]

$$E = -D \sum_{i,j} \frac{3(\hat{s}_i \cdot \hat{r}_{ij})(\hat{s}_j \cdot \hat{r}_{ij}) - \hat{s}_i \cdot \hat{s}_j}{r_{ij}^3} - KV \sum_i (\hat{s}_i \cdot \hat{e}_i)^2 - H\mu \sum_i \hat{s}_i \cdot \hat{H}, \tag{3}$$

where $D = \mu_0 \mu^2 / 4\pi a^3$ represents the dipolar strength, $K$ is the anisotropy constant, and $\hat{e}_i$ is its easy axis. $\vec{r}_{ij}$ is the distance separating particles $i$ and $j$ in units of $a$, $H$ is the strength of the applied magnetic field, and $\hat{H}$ is its direction. The magnetic properties of the assembly are dictated by the ratio $\Theta = D/KV$ rather than the precise values of parameters such as $d$, $a$, $M_s$, or $K$.

### B. Resistor network method

The resistance of the MNP array is evaluated by representing it as a resistor network (RN) and solving the resulting system of current and voltage equations [7]. If $\phi_i$ is the potential at site $i$, charge conservation at each node requires that $\sum_{j=1}^{N} \sigma_{ij}(\phi_i - \phi_j) = 0$, where $\sigma_{ij}$ is as given by Eq. (1). Recall that the resistance decays exponentially with interparticle separation. For analytical tractability, it is therefore customary to consider only tunneling events between the $Q$ nearest-neighbor (NN) spins and neglect the cotunneling between farther sites [7,16]. If the opposite ends of the assembly are attached to electrodes, then the set of linear equations can be solved to obtain the potentials $\{\phi_i\}$, by using the boundary conditions $\phi_i = V_0$ if $i \in A$ and $\phi_i = 0$ if $i \in C$, where $A$ and $C$ represent the anode and the cathode. The conductance of the *assembly* is then given by $\sigma = \sum_{i,j} \sigma_{ij}(\phi_i - \phi_j)^2 / 2V_0^2$.

### C. Statistical averages method

A more popular but less accurate method is where the magnetoresistance is evaluated by a statistical average of the cosine (SAC) [6,16]. In this case, the average conductance is given by $\langle \sigma \rangle \propto (1 + P^2 \langle \cos\theta \rangle)$, where $\langle \cos\theta \rangle$ represents a statistical average of $\cos\theta_{ij}$ over all NN spin pairs. Using Eq. (2), it is easy to see that

$$\mathrm{MR}(H) = \frac{\langle \cos\theta \rangle_{H_S} - \langle \cos\theta \rangle_H}{P^{-2} + \langle \cos\theta \rangle_H}. \tag{4}$$

To maximize TMR amplitude, the extremal values of $\langle \cos\theta \rangle$ should be as far apart as possible. This happens when the moments exhibit an antiparallel alignment at $H$ and a parallel alignment at the saturating field value $H_S$ yielding the maximum amplitude of $2P^2/(1-P^2)$. The spin polarization $P$ therefore sets the scale of the maximum value of TMR.

### D. Tunnel magnetoresistance ratio

Although Eq. (2) is conventionally used in the literature, the resulting TMR value is not bounded, i.e., for $P = 1$ the maximum amplitude is $\infty$. This makes it difficult to compare the TMR across different system parameters. A convenient definition is

$$\mathrm{MR}(H) = \frac{\sigma(H_s) - \sigma(H)}{\sigma(H_s)}. \tag{5}$$

This definition yields a maximum TMR amplitude of 1 for $P = 1$ and we use it in the rest of our paper. However, we shall also mention the TMR values obtained with the definition of Eq. (2), where necessary, for comparison. It is pertinent to point out here that although the *resistance* of an array of nanoparticles has an exponential dependence on the interparticle distance, the TMR amplitude in most cases weakly depends on it [25,26].

### E. Simulation details

To obtain the spin configuration $\{\hat{s}_i\}$ of the MNPs, we perform MC simulations using the standard Metropolis

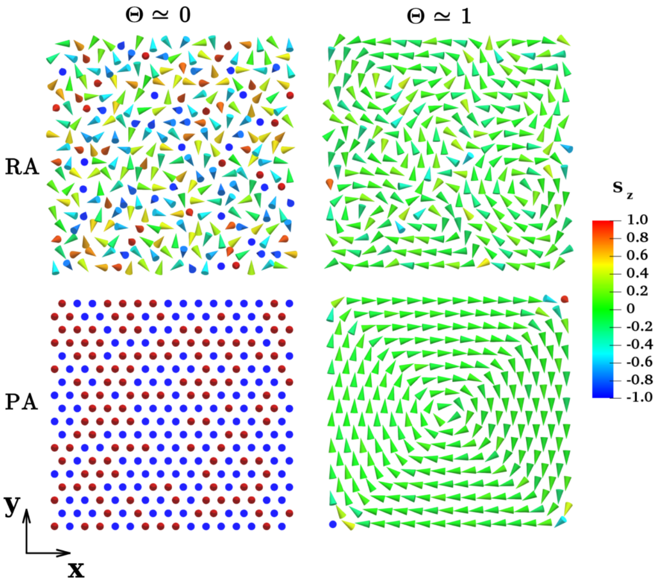

FIG. 1. Typical zero-field spin morphologies of square arrays ($16a \times 16a$) for weak coupling $\Theta \simeq 0$ (left) and strong coupling $\Theta \simeq 1$ (right). The top and bottom rows correspond to samples with random anisotropy (RA) and perpendicular anisotropy (PA), respectively. The moments (cones) are colored based on the $z$ component $s_z$.

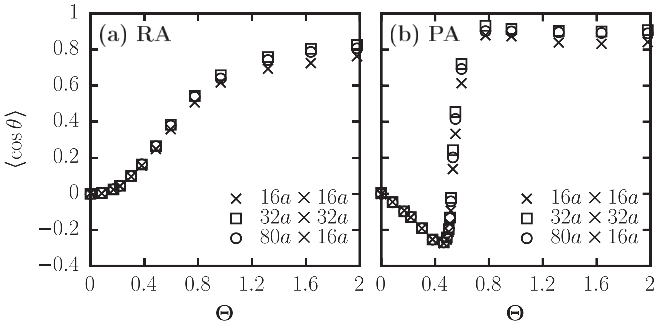

FIG. 2. $\langle\cos\theta\rangle$ as a function of $\Theta$ for different sample sizes. MNPs have (a) random anisotropy (RA) axes and (b) perpendicular anisotropy (PA) axes.

algorithm. Although the Metropolis MC method is an equilibrium sampling scheme, it is sufficient for our study as TMR measurements are usually performed in the timescale of a few minutes, where the system has enough time to equilibrate. Furthermore, studies comparing Langevin dynamics simulations with MC methods have shown that at timescales longer than the spin precession time, both the methods are equivalent [27,28]. For the simulations, we used triangular lattices of size $16a \times 16a$ and $32a \times 32a$ with free boundary conditions. Dipolar energy is evaluated explicitly without any cutoffs. The reduced temperature $t = k_BT/KV$ was kept constant at 0.0064, corresponding to typical experiments on superparamagnetic particles at low temperature or ferromagnetic particles at room temperature [20–22]. Unless otherwise stated, we used $P = 1$ for TMR calculations. Two distinct orientations of the anisotropy axes were considered: random anisotropy (RA) where $\{\hat{e}_i\}$ are oriented at random, and perpendicular anisotropy (PA) where $\{\hat{e}_i\}$ are oriented along the $z$ direction. The systems were allowed to equilibrate for 16 000 MC sweeps and the thermal averages were calculated over the subsequent 8000 MC sweeps. Each data set has been averaged over 50 independent runs corresponding to different random initial orientations of $\{\hat{s}_i\}$. We do not show error bars as they are smaller than the symbols.

## III. RESULTS AND DISCUSSION

### A. Zero-field morphologies

Typical zero-field spin morphologies of square arrays ($16a \times 16a$) are depicted in Fig. 1. For the RA configurations (top row), when the dipolar coupling is weak ($\Theta \simeq 0$), the zero-field morphologies are comprised of randomly oriented magnetic moments. For $\Theta = 1$, there is in-plane alignment accompanied by the formation of flux closure loops. The average magnetization of such states is $\simeq$0. For the PA configuration (bottom row), when $\Theta \lesssim 0.5$, the zero-field morphologies are composed of moments pointing perpendicular to the plane of the array, with roughly half of them pointing in the $+z$ and $-z$ directions. As $\Theta$ is increased, there is an abrupt reorientation transition at $\Theta = \Theta_r \simeq 0.5$ above which the moments lie in the $xy$ plane (bottom right panel). This is similar to the reorientation transition observed in thin films with perpendicular anisotropy and corresponds to the point where the shape anisotropy of the MNP array overcomes perpendicular anisotropy. In the case of RA on the other hand, the in-plane alignment of spins with increasing $\Theta$ is continuous. In both cases, samples with aspect ratio greater than 1 and strong dipolar coupling ($\Theta \geqslant 1$) exhibited increased alignment of moments along the length of the sample. To understand the local ordering of the moments better, we show in Fig. 2 the plots of $\langle\cos\theta\rangle$ as a function of $\Theta$ for different sample sizes. For the RA configuration [Fig. 2(a)], with increasing $\Theta$ there is a gradual increase in $\langle\cos\theta\rangle$ as local order sets in. For the PA configuration [Fig. 2(b)] there is a decrease in $\langle\cos\theta\rangle$, which becomes negative, up to the reorientation point $\Theta_r \simeq 0.5$. This corresponds to a progressive building of an antiparallel state of magnetic moments. Beyond the reorientation point, the moments become ferromagnetically aligned in plane giving $\langle\cos\theta\rangle \simeq 1$.

### B. Hysteresis and TMR with in-plane field

Next, we discuss magnetic hysteresis and TMR response of these arrays. The magnetization of the array is defined as $\vec{m} = m_x\hat{x} + m_y\hat{y} + m_z\hat{z}$, with $m_\alpha = \frac{1}{N}\sum_i\langle(s_i)_\alpha\rangle$, where $\alpha \in \{x, y, z\}$. In Fig. 3, we show the plots of $m_x$ and TMR for square arrays ($32a \times 32a$), with an in-plane field $\vec{h} = h_x\hat{x}$, and different values of $\Theta$. Here, $h = |\vec{h}| = H\mu/KV$ represents the reduced field, and the TMR has been evaluated using the RN model. Let us first discuss the case of samples with RA [Figs. 3(a) and 3(c)]. For $\Theta = 0$, the hysteresis is well described by the Stoner-Wohlfarth model [29]. The remanent magnetization $m_r = 0.5$ and the coercive field $h_c = 1$, as expected. As $\Theta$ is increased, $m_r$ increases and $h_c$ decreases in accordance with earlier studies [13,30]. However, for large dipolar strength ($\Theta \geqslant 1$), the formation of flux closure loops decreases $m_r$ and increases the saturation field. This

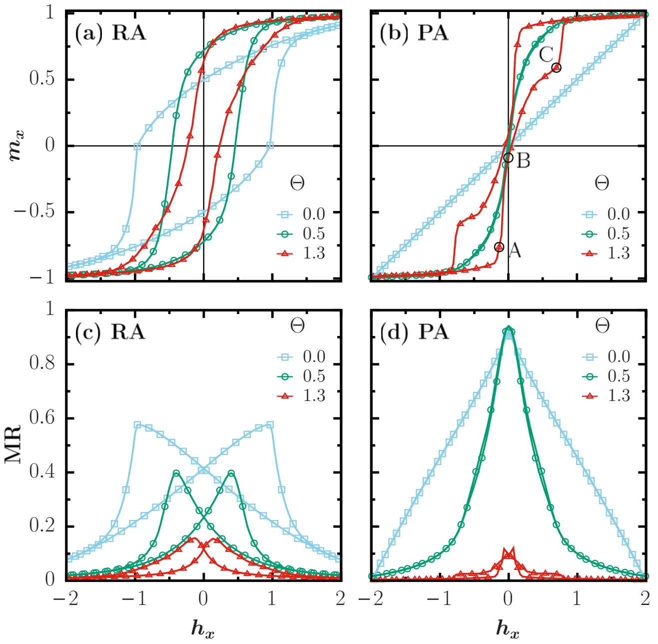

FIG. 3. Hysteresis and TMR behavior of square arrays ($32a \times 32a$) for a field applied along $\hat{x}$. Panels (a) and (c) are for the RA configuration and (b) and (d) are for the PA configuration. The TMR was calculated using the RN method and with the definition given in Eq. (5).

nonmonotonic behavior of $m_r$ with Θ was also observed in the simulations performed by Tan *et al.* [16]. The TMR response is maximized for $\Theta = 0$, with the maximum value of $\simeq 0.575$ occurring near the coercive field $h_c$. As Θ is increased, the morphologies become more and more locally ordered (see Fig. 1), and the TMR response decreases.

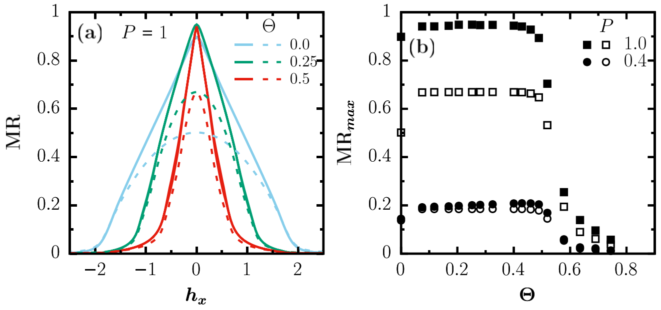

FIG. 5. (a) TMR curves obtained using the RN method (solid lines) and the SAC method (dashed lines) for $32a \times 32a$ array in PA configuration. The TMR is defined as given in Eq. (5). (b) $\mathrm{MR}_{max}$ as a function of Θ evaluated using the RN method (filled symbols) and the SAC method (open symbols). RN gives the correct behavior.

For the PA configuration [Figs. 3(b) and 3(d)], when $\Theta < \Theta_r$, the magnetization plots do not show any hysteresis, as the reorientation of spins from out-of-plane to in-plane alignment is favored by the dipolar field. Interestingly, a large TMR response is observed with a maximum value $\simeq 0.96$. This is close to the perfect TMR amplitude 1, and is due to the large number of NN antiparallel spin pairs at the coercive field. In terms of the conventional definition [Eq. (2)], this would correspond to a TMR amplitude of 24 (or 2400%). For $\Theta > \Theta_r$, the spins are aligned in plane and form flux closure loops. The drop in magnetization at point A marks the formation of flux loops which are the natural low-energy configurations. These proliferate in the sample with reducing field (point B). As the field becomes positive, they are pushed toward the edges of the sample, perpendicular to the direction of applied field (point C). The flux loops present a large energy barrier to the system, and their removal is reflected by a jump in the magnetization. Figure 4 shows snapshots of typical spin configurations at the points A, B, and C. Further, there is an increase in both $m_r$ and $h_c$, and the TMR amplitude is dramatically reduced due to increased local order.

We now provide more details on the PA configuration, which displays the largest TMR amplitude. In Fig. 5(a) we show MR as a function of the in-plane field $\vec{h} = h_x\hat{x}$, for a $32a \times 32a$ array in the PA configuration, evaluated using the RN method (solid lines) and the SAC method (dashed lines). We find a large difference in the TMR values obtained from the two methods. This is because the net resistance of the array depends on the distribution of resistances across the network. The SAC method does not account for this, whereas the RN method explicitly solves Kirchoff's current and voltage equations for the network. Therefore, the RN method gives the more realistic and accurate measure of the array conductivity. An extreme example of this is when $P = 1$, where antiparallel spin pairs have zero conductance. If there are no percolating paths of conducting spin pairs across the array, it is possible to have *zero* net conductance. In this case, the SAC method will

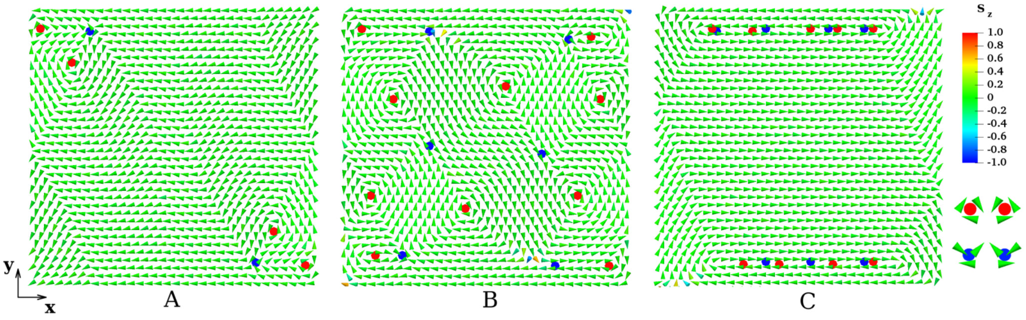

FIG. 4. Snapshots of spin configurations at points A, B, and C shown in the hysteresis loop of Fig. 3(b). The moments (cones) are colored according to their $z$ component. Solid red (blue) circles mark the positions about which spins in a closed loop undergo a $+2\pi$ $(-2\pi)$ rotation, as illustrated alongside.

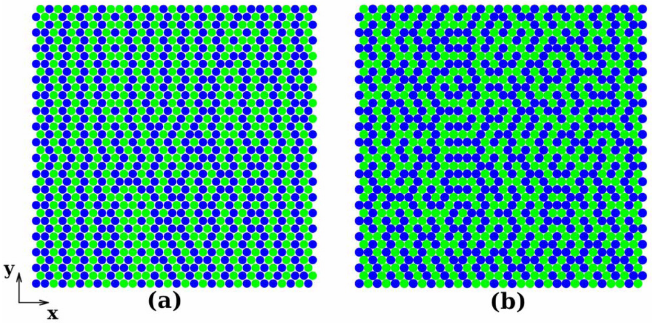

FIG. 6. Snapshots showing the typical spin morphologies at the coercive field on triangular lattice with perpendicular anisotropy for (a) a nearest-neighbor antiferromagnet and (b) spins with dipole-dipole interactions. The strength of the exchange interaction $J_{ex} = 0.325KV$ and dipolar interaction $D = 0.325KV$. The magnetic field was applied along the $x$ axis. The green dots indicate particles with $S_z = 1$ while the blue dots represent $S_z = -1$.

predict a nonzero value of the average cosine resulting in a *nonzero* conductivity! In Fig. 5(b) we show the corresponding peak value of the TMR ratio $\mathrm{MR}_{max}$ as a function of $\Theta$ for $P = 0.4$ and 1.0, evaluated using the RN method (filled symbols) and the SAC method (open symbols). Note that the TMR amplitude does not go through a maximum as it might have been expected from Fig. 2(b). This is because during field cycling, for $\Theta < \Theta_r$, the $\langle\cos\theta\rangle$ value at the coercive field is roughly independent of $\Theta$, and is lower ($-0.34$) than the corresponding zero-field value at $\Theta_r$ ($-0.27$). Consequently, the states at $h_c$ are more antiferromagnetic (AF) than at zero field, leading to a higher than expected TMR response.

One could naively argue that with PA, the system is expected to have a disordered AF state at the coercive field, so a large TMR response is not surprising. However, it is not so trivial as AF interactions on a triangular lattice can often result in the formation of stripe patterns [31,32]. This is demonstrated in Fig. 6(a) which shows the equilibrium spin morphology obtained from an MC simulation of a triangular lattice with NN AF interactions and PA at the coercive field. The green dots indicate particles with $S_z = 1$ while the blue dots represent $S_z = -1$. Notice the formation of stripes or correlated regions of $+1$ and $-1$, with many spanning the lattice in the $y$ direction. Consequently, the TMR along the $y$ axis is only 60% of the maximal value. Figure 6(b), on the other hand, depicts the equilibrium morphology of the same system, with long-range dipolar interactions. Correlated regions are seen in this case as well, but they do no percolate the lattice. As a result, there are a large number of AF pairs $\sim O(N^2)$ which yield a very large TMR amplitude along *both* directions.

### C. Hysteresis and TMR with out-of-plane field

Next, we study the magnetization and TMR when the external field is applied perpendicular to the plane of the sample. For this case, we did not observe a significant dependence on the sample size or the aspect ratio. Figure 7 shows prototypical plots of $m_z$ and MR for a square array ($16a \times 16a$) with a perpendicular field $\vec{h} = h_z\hat{z}$, and different values of $\Theta$. For samples with RA [Figs. 7(a) and 7(c)], $\Theta = 0$ shows the expected Stoner-Wohlfarth behavior. As $\Theta$ increases, $m_r$ and $h_c$ decrease to zero. The absence of hysteresis for $m_z$ with increasing dipolar strength is because of the shape anisotropy of the array which opposes any magnetization perpendicular to the plane of the array, and is a standard result of the Stoner-Wohlfarth model [33]. Similar to the case with in-plane field, the maximum TMR observed is 0.575 for $\Theta = 0$, and it reduces with increasing $\Theta$ due to local ordering. For samples with PA [Figs. 7(b) and 7(d)], when $\Theta = 0$, the hysteresis shows a sharp switching from an "all-down" to "all-up" configuration (or vice versa) at $h = h_c = 2$. As $\Theta$ increases, local order sets in and $m_r$ and $h_c$ decrease. Magnetization reversals are seen as "steps" in the hysteresis curve: at each step a fraction of the spins flip, as also observed by Xu *et al.* [34]. For $0 < \Theta \leqslant \Theta_r$, a large TMR response is observed with a maximum value $\simeq$0.96. This is similar to the case with in-plane field, except that a hysteresis is observed here. The steps in the hysteresis are reflected in the TMR response as well. For $\Theta > 0.5$, the TMR ratio is less than 0.1. For both RA and PA, large fields are required to magnetize the system in the perpendicular direction, as the dipolar field tends to align moments in plane.

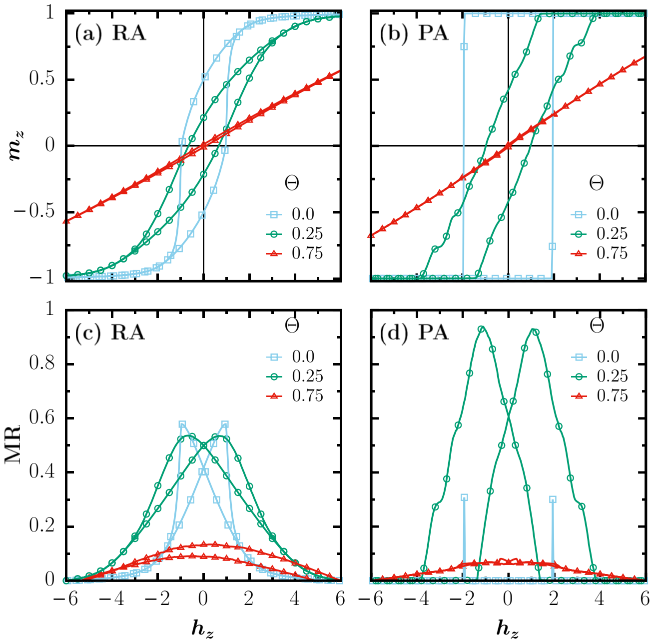

FIG. 7. Hysteresis and TMR behavior of square arrays ($16a \times 16a$) with the applied field along $\hat{z}$. Panels (a) and (c) are for the RA configuration and (b) and (d) are for the PA configuration. The TMR was calculated using the RN method and with the definition given in Eq. (5).

### D. Effect of sample size and aspect ratio

In Fig. 8, we show the plots of $m$ as a function of in-plane field, for $\Theta = 1.3$ and different sample sizes. The sample size and the direction of the in-plane field are mentioned in the plot legend. Figures 8(a) and 8(c) are for the RA configuration. Figures 8(b) and 8(d) are for the PA configuration. We make the following common observations: (i) For smaller arrays,

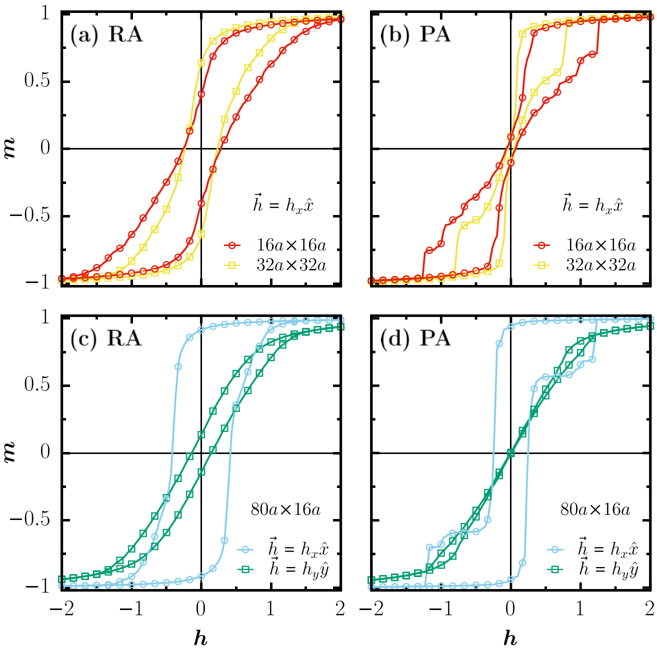

FIG. 8. Effect of sample size and aspect ratio on the hysteresis curves for $\Theta = 1.3$, and an in-plane field. The sample size and the field directions are mentioned in the plot legend.

there is a decrease in the remanent magnetization $m_r$ and a slight increase in the coercive field $h_c$. (ii) For elongated samples, $m_r$ and $h_c$ are reduced when the field is applied perpendicular to the long side of the array, whereas they increase when the field is applied parallelly.

These features are reflected in the TMR curves as well, i.e., the peak of the TMR curve shifts with the coercive field, however, the amplitude is not affected significantly. We do not depict the TMR curves here. For an out-of-plane magnetic field, we did not observe any significant dependence of hysteresis or TMR response on sample size and aspect ratio.

### E. Materials and parameters for maximizing TMR

Finally, we provide an analysis on how these large TMR amplitudes could be observed experimentally at room temperature. There are three requisites to achieve this goal: (i) $\Theta < 0.5$, (ii) blocking temperature $T_b > 300$ K, and (iii) $P \simeq 1$. The latter is satisfied by half-metals such as $X$MnSb ($X$ = Pt, Ni, Co, Au, Cu), PtMnSn, $Mn_2Ru_xGa$, $Co_2FeX$ ($X$ = Al, Si), and $Fe_3O_4$ [35–40]. We have estimated the possibility of achieving criteria (i) and (ii) for four different materials of interest (Fe, CoPt, $Fe_3O_4$, and NiMnSb). Table I provides the results of calculations estimating the suitability of various materials to obtain large TMR amplitudes and their required shapes. The nano-objects have been assumed to be either spheres or 60-nm-tall nanorods. The anisotropy value taken for the spheres is the bulk magnetocrystalline anisotropy of the material, and for nanorods, the shape anisotropy amplitude of $K \simeq \mu_0 M_S^2/4$ has been used [41]. The diameter $d$ for which $\Theta < 0.5$ has been calculated using the equations provided in Sec. II. The tunnel barrier thickness or the interparticle spacing is given by $s$. The blocking temperature $T_b$ of the nano-objects has been calculated using the standard equation $T_b = KV/25k_B$ [41]. The rightmost column gives the suitability of a given material of a given shape to obtain $T_b > 300$ K as well as $\Theta < 0.5$ at the same time.

We find that for a large magnetocrystalline anisotropy material such as CoPt, it is relatively easy to achieve $\Theta < 0.5$ and $T_b > 300$ K even for spheres of a few nm. On the other hand, for materials like Fe, $Fe_3O_4$, and NiMnSb, it is shown that nanorods of a few nm in diameter would work. For a low anisotropy and low magnetization material such as $Fe_3O_4$, the tunnel barrier thickness (which modifies $\Theta$) surrounding the nanorods has to be increased to 5 nm to fulfill these conditions, whereas for Fe and NiMnSb, tunnel barriers of 3 or 4 nm are sufficient. Regarding the possibility of fabricating such heterostructures, several groups have developed oriented growth techniques or deposition under magnetic field to grow magnetic nanoparticles, nanorods, or nanowires with their easy axis perpendicular to the substrate [42–46]. Thus, by a careful choice of material parameters, large TMR amplitudes could be achieved in triangular MNP arrays.

## IV. SUMMARY

We conclude this paper with a summary of our results and their implications for experiments. In this work, we have studied the hysteresis and TMR behavior of a system of MNPs

TABLE I. Nanoparticle diameter $d$ and interparticle spacing $s$ required to achieve $\Theta < 0.5$ for different magnetic materials and different anisotropy types. Also listed are the corresponding blocking temperatures $T_b$ and hence the suitability of these materials for achieving maximum TMR at room temperature.

| Material | Nano-object | Anisotropy | $s$ | $d$ for $\Theta < 0.5$ | $T_b$ | Suitable |
|---|---|---|---|---|---|---|
| Fe | Sphere | Magnetocrystalline | 3 nm | $d < 3.5$ nm | 3 K for $d = 3.5$ nm | No |
| | Nanorod | Shape | 3 nm | $d < 2.1$ nm | 550 K for $d = 2.1$ nm | Yes |
| $Fe_3O_4$ | Sphere | Magnetocrystalline | 3 nm | $d < 14$ nm | 54 K for $d = 14$ nm | No |
| | Nanorod | Shape | 3 nm | $d < 2.1$ nm | 41 K for $d = 2.1$ nm | No |
| | Nanorod | Shape | 4 nm | $d < 4.6$ nm | 200 K for $d = 4.6$ nm | No |
| | Nanorod | Shape | 5 nm | $d < 8$ nm | 600 K for $d = 8$ nm | Yes |
| CoPt | Sphere | Magnetocrystalline | 3 nm | any $d$ | 300 K for $d = 3.5$ nm | Yes |
| NiMnSb | Sphere | Magnetocrystalline | 3 nm | $d < 5.6$ nm | 3.5 K for $d = 5.6$ nm | No |
| | Nanorod | Shape | 3 nm | $d < 2.1$ nm | 85 K for $d = 2.1$ nm | No |
| | Nanorod | Shape | 4 nm | $d < 4.6$ nm | 410 K for $d = 4.6$ nm | Yes |

on triangular lattice, interacting via dipole interactions. For MNPs with random anisotropy orientations, the maximum TMR achieved is $P^2$ in the limit of zero interactions, and decreases with increasing dipolar strength. In contrast, we find that MNPs with perpendicular anisotropy display a near-ideal TMR of $\sim 2P^2/(1-P^2)$ [according to Eq. (2)] when $\Theta$, the ratio of dipole interaction strength to anisotropy strength, is less than 0.5. With the right materials, the TMR amplitude could be as large as 2400%. This is an order of magnitude improvement over previous studies [7,16,17]. We have also provided the conditions under which these maximal amplitudes could be obtained experimentally at room temperature. We hope that experimentalists will be inspired by our work and will create such arrays and superlattices.

## ACKNOWLEDGMENTS

Financial support from the Indo-French Centre for the Promotion of Advanced Research and from HPC facility at IIT Delhi is acknowledged.

---

[1] C. Petit, A. Taleb, and M.-P. Pileni, Adv. Mater. **10**, 259 (1998).

[2] C. Black, C. Murray, R. Sandstrom, and S. Sun, Science **290**, 1131 (2000).

[3] B. Van Waeyenberge, A. Puzic, H. Stoll, K. W. Chou, T. Tyliszczak, R. Hertel, M. Fähnle, H. Brückl, K. Rott, G. Reiss, I. Neudecker, D. Weiss, C. H. Black, and G. Schütz, Nature (London) **444**, 461 (2006).

[4] S. Sun, Adv. Mater. **18**, 393 (2006).

[5] R. P. Cowburn, Nat. Mater. **6**, 255 (2007).

[6] J. Inoue and S. Maekawa, Phys. Rev. B **53**, R11927 (1996).

[7] D. Kechrakos and K. N. Trohidou, Phys. Rev. B **71**, 054416 (2005).

[8] L. F. Zhang, C. Xu, P. M. Hui, and Y. Q. Ma, Eur. Phys. J. B **52**, 305 (2006).

[9] J. J. Weis, Mol. Phys. **100**, 579 (2002).

[10] P. Politi, M. G. Pini, and R. L. Stamps, Phys. Rev. B **73**, 020405(R) (2006).

[11] V. Russier, J. Appl. Phys. **89**, 1287 (2001).

[12] V. Russier, C. Petit, J. Legrand, and M. P. Pileni, Phys. Rev. B **62**, 3910 (2000).

[13] G. A. Held, G. Grinstein, H. Doyle, S. Sun, and C. B. Murray, Phys. Rev. B **64**, 012408 (2001).

[14] P. Poddar, T. Telem-Shafir, T. Fried, and G. Markovich, Phys. Rev. B **66**, 060403(R) (2002).

[15] F. Luis, F. Petroff, J. M. Torres, L. M. García, J. Bartolomé, J. Carrey, and A. Vaurès, Phys. Rev. Lett. **88**, 217205 (2002).

[16] R. P. Tan, J. S. Lee, J. U. Cho, S. J. Noh, D. K. Kim, and Y. K. Kim, J. Phys. D: Appl. Phys. **43**, 165002 (2010).

[17] Z. Mao and X. Chen, J. Phys. D: Appl. Phys. **43**, 425001 (2010).

[18] M. Anand, J. Carrey, and V. Banerjee, J. Magn. Magn. Mater. **454**, 23 (2018).

[19] W. Wang, M. Yu, M. Batzill, J. He, U. Diebold, and J. Tang, Phys. Rev. B **73**, 134412 (2006).

[20] R. P. Tan, J. Carrey, C. Desvaux, J. Grisolia, P. Renaud, B. Chaudret, and M. Respaud, Phys. Rev. Lett. **99**, 176805 (2007).

[21] J. Dugay, R. P. Tan, A. Meffre, T. Blon, L.-M. Lacroix, J. Carrey, P. F. Fazzini, S. Lachaize, B. Chaudret, and M. Respaud, Nano Lett. **11**, 5128 (2011).

[22] J. Dugay, R. P. Tan, M. Ibrahim, C. Garcia, J. Carrey, L.-M. Lacroix, P.-F. Fazzini, G. Viau, and M. Respaud, Phys. Rev. B **89**, 041406(R) (2014).

[23] S. Usmani, M. Lepesant, A. Bupathy, T. Blon, L.-M. Lacroix, V. Banerjee, B. Chaudret, and J. Carrey, Phys. Rev. B **98**, 104433 (2018).

[24] D. Kechrakos and K. N. Trohidou, J. Nanosci. Nanotechnol. **8**, 2929 (2008).

[25] J. Hayakawa, S. Ikeda, F. Matsukura, H. Takahashi, and H. Ohno, Jpn. J. Appl. Phys. **44**, L587 (2005).

[26] J. Du, W. T. Sheng, L. Sun, B. You, M. Lu, A. Hu, X. H. Xiang, and J. Q. Xiao, J. Magn. Magn. Mater. **277**, 90 (2004).

[27] U. Nowak, R. W. Chantrell, and E. C. Kennedy, Phys. Rev. Lett. **84**, 163 (2000).

[28] P. V. Melenev, Y. L. Raikher, V. V. Rusakov, and R. Perzynski, Phys. Rev. B **86**, 104423 (2012).

[29] E. C. Stoner and E. Wohlfarth, Philos. Trans. R. Soc. London A **240**, 599 (1948).

[30] D. Kechrakos and K. N. Trohidou, Phys. Rev. B **74**, 144403 (2006).

[31] G. H. Wannier, Phys. Rev. **79**, 357 (1950).

[32] M. M. Hurley and S. J. Singer, Phys. Rev. B **46**, 5783 (1992).

[33] J. J. Lu, H. L. Huang, and I. Klik, J. Appl. Phys. **76**, 1726 (1994).

[34] C. Xu, P. M. Hui, L. F. Zhang, Y. Q. Ma, J. H. Zhou, and Z. Y. Li, Eur. Phys. J. B **46**, 475 (2005).

[35] R. A. de Groot, F. M. Mueller, P. G. van Engen, and K. H. J. Buschow, Phys. Rev. Lett. **50**, 2024 (1983).

[36] P. G. van Engen, K. H. J. Buschow, R. Jongebreur, and M. Erman, Appl. Phys. Lett. **42**, 202 (1983).

[37] H. van Leuken and R. De Groot, Phys. Rev. Lett. **74**, 1171 (1995).

[38] C. M. Fang, G. A. de Wijs, and R. A. de Groot, J. Appl. Phys. **91**, 8340 (2002).

[39] K. Borisov, D. Betto, Y.-C. Lau, C. Fowley, A. Titova, N. Thiyagarajah, G. Atcheson, J. Lindner, A. M. Deac, J. M. D. Coey, P. Stamenov, and K. Rode, Appl. Phys. Lett. **108**, 192407 (2016).

[40] A. Boehnke, U. Martens, C. Sterwerf, A. Niesen, T. Huebner, M. von der Ehe, M. Meinert, T. Kuschel, A. Thomas, C. Heiliger, M. Münzenberg, and Günter Reiss, Nat. Commun. **8**, 1626 (2017).

[41] J. M. D. Coey, *Magnetism and Magnetic Materials* (Cambridge University Presss, New York, 2010).

[42] Y.-C. Wu, L.-W. Wang, and C.-H. Lai, Appl. Phys. Lett. **93**, 242501 (2008).

[43] J.-M. Qiu, J. Bai, and J.-P. Wang, Appl. Phys. Lett. **89**, 222506 (2006).

[44] L. Vayssieres, L. Rabenberg, and A. Manthiram, Nano Lett. **2**, 1393 (2002).

[45] N. Liakakos, T. Blon, C. Achkar, V. Vilar, B. Cormary, R. P. Tan, O. Benamara, G. Chaboussant, F. Ott, B. W.-Fonrose, E. Snoeck, B. Chaudret, K. Soulantica, and M. Respaud, Nano Lett. **14**, 3481 (2014).

[46] K. Watanabe, B. Jinnai, S. Fukami, H. Sato, and H. Ohno, Nat. Commun. **9**, 663 (2018).